Self-organization of Cu–Ag during controlled severe plastic deformation at high temperatures

Salman N. Arshad
Department of Materials Science and Engineering, University of Illinois at Urbana Champaign, Urbana, Illinois 61801, USA; and Department of Chemistry, Syed Babar Ali School of Science and Engineering, Lahore University of Management Sciences, Lahore 54792, Pakistan

Timothy G. Lach
Department of Materials Science and Engineering, University of Illinois at Urbana Champaign, Urbana, Illinois 61801, USA

Julia Ivanisenko
Institute for Nanotechnology, Karlsruhe Institute for Technology (KIT), 76344 Eggenstein-Leopoldshafen, Germany

Daria Setman
Department of Physics, University of Vienna, A-1090 Vienna, Austria

Pascal Bellon, Shen J. Dillon,[a] and Robert S. Averback
Department of Materials Science and Engineering, University of Illinois at Urbana Champaign, Urbana, Illinois 61801, USA

(Received 9 November 2014; accepted 14 April 2015)

$Cu_{90}Ag_{10}$ alloys were subjected to severe plastic deformation at temperatures ranging from 25 to 400 °C and strain rates ranging from 0.1 to 6.25 s^{-1} using high-pressure torsion. The deformed samples were characterized by x-ray diffraction, transmission electron microscopy, and atom-probe tomography. A dynamic competition between shear-induced mixing and thermally activated decomposition led to the self-organization of the Cu–Ag system at length scales varying from a few atomic distances at room temperature to ≈50 nm at 400 °C. Steady-state microstructural length scales were minimally affected by varying the strain rate, although at 400 °C, the grain morphology did depend on strain-rate. Our results show that diffusion below 300 °C is dominated by nonequilibrium vacancies, and by comparison with previous Kinetic Monte Carlo simulations [D. Schwen et al., *J. Mater. Res.* **28**, 2687–2693 (2013)], their concentration could be obtained.

I. INTRODUCTION

Thermo-mechanical alloy design and processing typically impose mechanical, thermal, or chemical driving forces on a system that promote the formation and evolution of nonequilibrium point and planar defects, and in some cases, chemical disorder. Desired microstructures are subsequently obtained through controlled relaxations toward lower energy states during thermal annealing. At the relatively low strains and strain rates associated with most commercial thermo-mechanical alloy processing, the transient behavior of line and planar defects, and their interactions with various atomic and microstructural features, tends to dominate the overall microstructural response and to dictate materials properties. The low production of nonequilibrium point defects at small strains tends to make their contribution to microstructural evolution rather insignificant, at least in terms of affecting microstructural design parameters like grain size and phase stability. Similarly, the spatial dimensions over which nonequilibrium forced chemical mixing occurs tend to be insignificant at relatively low strains in coarse microstructures. In contrast, processing alloys at large strain rates, and to much higher levels of strain, often with the goal of nanostructuring, heightens the importance of understanding the behavior of nonequilibrium point and chemical defects as their concentrations can significantly exceed the concentrations of intrinsic defects. Few detailed experimental studies, however, have investigated this processing regime under conditions where temperature, high strain, and high continuous strain rate are accurately controlled and well specified.

Forced chemical mixing at room temperature has received a great deal of attention over the past few decades in the context of severe plastic deformation (SPD), which is often associated with the high strains used to refine the microstructure toward the nanometer scale.[1–11] In the

Contributing Editor: Jürgen Eckert
[a]Address all correspondence to this author.
e-mail: sdillon@illinois.edu
DOI: 10.1557/jmr.2015.119

 © Materials Research Society 2015

https://doi.org/10.1557/jmr.2015.119 Published online by Cambridge University Press

absence of significant vacancy migration, the nature of forced atomic relocations in the bulk and at interfaces, governs chemical mixing and the spatial frequencies of compositional heterogeneities. Alloys with heats of mixing much less than zero often undergo chemical or structural disordering.[12] Miscible and moderately immiscible ($|\Delta H_{mix}|$ less than $\approx$15 kJ mol^{-1}) systems tend to chemically homogenize at sufficiently high strains while maintaining crystallinity.[10,13–16] Experiments, theory, and simulations indicate that in this case the strain required for homogenization scales approximately linearly with the characteristic wave length of the initial compositional heterogeneities.[17–20] Highly immiscible systems ($\Delta H_{mix} > 20$ kJ mol^{-1}) investigated in the literature typically remain phase separated at the nanoscale with only limited enhanced solubilities.[21–25] This behavior has been attributed, in some cases, to differences in local plasticity between the phases,[26,27] but also recently, to a thermo-chemical biasing in atom relocations during shear-induced mixing.[22,23,28,29] While the general trends described above have been demonstrated for a large number of alloys processed at temperatures below $\sim$0.25 T_{mp} (T_{mp} = melting temperature), the mechanisms controlling such behaviors still remain controversial. Comparable studies above $\sim$0.25 T_{mp} are far fewer (see Refs. 30–35 for several recent examples), despite the potential for developing new alloys with novel microstructures and properties within this processing space. The present study seeks to provide insights into the competition between forced atomic displacements occurring during SPD and vacancy mediated atomic relaxations in a model alloy, Cu–Ag. We choose Cu–Ag since shear mixing is well studied in this alloy at low temperatures and largely understood.[17,18,36–40]

Studies on high temperature SPD have been performed primarily using ball milling (BM), accumulative roll bonding, equal channel angular compression, and more recently with high pressure torsion (HPT).[4,30–35,41–43] For the alloy system to reach its steady state microstructure, however, only BM and HPT presently provide sufficiently high strain rates to be practical. Prior experiments used high temperature BM to investigate the microstructural evolution in nearly equiatomic Cu–Ag alloys (ΔH_{mix} $\sim$6 kJ mol^{-1} for $Cu_{50}Ag_{50}$ alloy).[13,44,45] These studies had shown that the alloy reaches a steady-state, multiphase microstructure at sufficiently high strain and that the characteristic length scales of this microstructure increase with increasing temperature. The apparent activation energies for phase decomposition were observed to be significantly smaller than those associated with vacancy migration: 0.66 and 0.7 eV in Ag and Cu, respectively. The studies provided differing explanations for the low apparent activation energy. In the earlier study, the measured activation energy, 0.11 eV, was interpreted in the context of first-order kinetics dominated by shear-induced vacancies.[13] In the subsequent work, a different measured apparent activation energy, 0.4–0.59 eV, was interpreted by a more complex combination of effects arising from saturated nonequilibrium vacancies, enthalpic effects resulting from concentrated solutions, and a convolution of lattice and grain boundary contributions.[45] Both of these studies have subsequently been interpreted more broadly within the context of steady-state self-organization, which can result when the length scales and time scales associated with forced chemical mixing compete with thermodynamic relaxations.[46,47] While these initial studies using high-temperature BM were key to establish the phenomenon of self-organized nanostructures in immiscible alloys under shear deformation, they lacked the necessary control of strain rate, total strain, and temperature to develop a quantitative understanding of this behavior. HPT, on the other hand, has emerged as a technique that offers high levels of strain, a strain rate that is both variable and controllable, and it is conducive to good temperature control[48–50]; we thus have utilized HPT in the present work to investigate the details of microstructural evolution in $Cu_{90}Ag_{10}$ alloys during SPD at elevated temperatures. The use of a relatively dilute alloy simplifies characterization of the length scale, as the Ag forms isolated nanoprecipitates in Cu,[17] which are easily identified by high-angle annular dark field scanning transmission electron microscopy (HAADF-STEM) imaging.

Shear-induced mixing is mediated in Cu–Ag predominantly through dislocation glide, as one plane of atoms glides past another plane. Such a so-called ballistic motion tends to homogenize the alloy. The highly correlated motion of atoms that occurs during shear mixing, however, is non-Fickian[17–20] and difficult to describe analytically. This motion, nevertheless, has been shown to be conveniently expressed in terms of the mean-square relative displacements of atoms, where the relative displacements between *pairs* of atoms are considered.[19] The relative pair diffusion rate,[51] moreover, has been predicted to scale linearly with the relative pair separation.[19] This result is easy to understand since a change in the relative position of two atoms requires the passage of a dislocation between them, and the probability for such an event increases linearly with their distance apart. At high temperatures, thermally activated diffusion also takes place, and it tends to return the system to equilibrium, where Cu–Ag is a two-phase alloy. Thus, shear mixing and thermally activated diffusion compete in determining the microstructure of the alloy. Since the shear-mixing rate increases linearly with length scale, and thermal diffusion is independent of length scale, it is intuitively clear that the alloy system should be able to order on small length scales where thermal diffusion dominates, while being disordered on large length scales, where ballistic mixing is dominant. Indeed, it was shown

https://doi.org/10.1557/jmr.2015.119 Published online by Cambridge University Press

that using Kinetic Monte Carlo (KMC) simulations (similar to Ref. 47) an immiscible alloy under combined shear mixing and thermal diffusion will phase separate on a length, r, which is given by the distance at which the two pair diffusion coefficients are equal,[47] i.e.,

$$r = \frac{a_0}{d^2}\frac{F_{\text{vac}}}{F_{\text{shear}}} \quad , \tag{1}$$

Here, F_{vac} is the frequency of vacancy jumps, F_{shear} is the frequency at which dislocations are inserted into the simulation cell, a_0 is the nearest neighbor distance, and d^2 is the number of atoms in a slip plane within the simulation cell. The simulations show, further, that the final length scale of the alloy microstructure is completely determined by the two dynamic state variables, F_{vac} and F_{shear}, and independent of the initial conditions. Dynamic phase diagrams can thus be constructed to characterize such driven systems.[52] While the model leading to Eq. (1) is highly idealized, it provides a convenient context for examining experimentally self-organization of immiscible alloys during SPD. This work thus utilizes HPT to investigate the effect of the two variables, temperature and strain rate, on microstructural development. We examine $Cu_{90}Ag_{10}$ alloy in the temperature range of ~0.12–~0.40 T_{mp}, at controlled strain rates varying between 0.1 and 6.25 s^{-1}.

II. EXPERIMENTAL

Chemically homogenized powders of $Cu_{90}Ag_{10}$ were first fabricated by high-energy BM (SPEX 8000 with hardened steel vial and milling balls) of micrometer-sized elemental Cu and Ag powders in an Ar-filled dry glove box. Atom probe tomography (APT), discussed below, indicates <1 at.% Fe impurity incorporation during BM. These powders were subsequently hot-pressed at 300 °C in a vacuum (2×10^{-6} Pa) under a pressure of ≈1 GPa, in a press attached directly to the glove box. The powder samples were not exposed to atmosphere prior to densification. The process resulted in >98% dense Cu rods, ≈ 10 mm in diameter, which contained Ag precipitates with a volume-averaged initial diameter, $D_{\text{p,i}}$, of 31 ± 7 nm. Annealing the as-pressed samples at 600 and 750 °C for 1 h in Ar increased the precipitate sizes to $D_{\text{p,i}}$ of 122 ± 25 nm and 252 ± 58 nm, respectively. Particle size was determined by tracing individual Ag particles, as identified by a combination of concurrently acquired bright-field scanning transmission electron microscopy (BF-STEM) and HAADF-STEM images, using ImageJ software. The associated error bars are one standard deviation of the particle diameter distributions measured over 200 particles. The particle size distributions of the as-prepared samples are log-normal, as expected. The samples were cut into 250 μm thick disks, polished, and then deformed by back and forth (+90°/−90°) HPT cycles in the "unconstrained" configuration, i.e., the sample was compressed between flat anvils, thereby allowing the sample to flow outward. The thinness of the samples and high friction, however, prevents significant flow; the change in thickness is only ≈20%. This sample geometry and HPT configuration were previously optimized so that deformation is nearly homogeneous through thickness.[17] HPT was performed at 0.1, 1, and 6 rpm under a pressure of 4.5 GPa at temperatures of 125, 200, 300, and 400 °C. The temperature of the anvils, whose thermal mass far exceeds that of the sample, was controlled to maintain the processing temperature. The temperature of the sample was monitored with a pyrometer (± 0.5 °C at 400 °C) adjacent to the sample position. HPT was initiated immediately after inserting the samples, and the samples quenched at the end of the cycle. High temperature BM was also performed at 125, 200, 300, and 400 °C using fully mixed $Cu_{90}Ag_{10}$ powders, mixed powders after 600 °C annealing, and micrometer-sized elemental powders as the starting material. A heating tape was wrapped around the vial in the BM to raise the temperature, and a control thermocouple was attached to the outer surface. It is noted that the internal temperature of the vial may deviate somewhat from the temperature at its surface; however, we expect that the quoted temperature values are sufficiently accurate to provide a reasonable comparison with the HPT samples.

We begin by defining a reference frame for the samples, as HPT deforms the sample anisotropically. This is shown in Fig. 1 (here, ND = normal direction, RD = radial direction, and TD = transverse direction). HAADF-STEM (JEOL 2200FS) and APT (Cameca LEAP 4000X Si, Northwestern University)[53] were performed on samples prepared by focused ion beam (FEI company) milling. TEM samples were prepared for observation along the ND and TD directions, and atom probe needles were aligned along the ND direction. APT samples having 40–50 nm tip radii were analyzed at

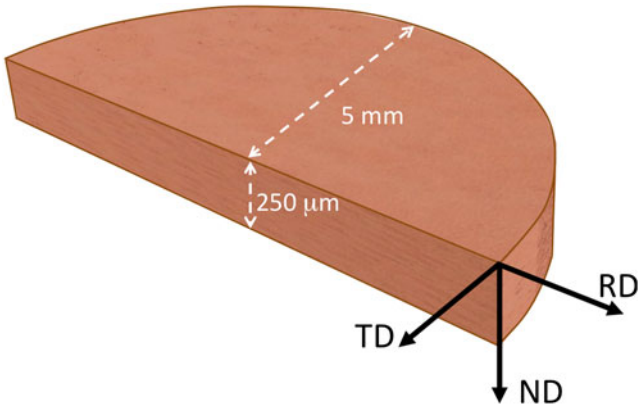


FIG. 1. Cross-sectional schematic of sample geometry with sample reference frame directions depicted.

https://doi.org/10.1557/jmr.2015.119 Published online by Cambridge University Press

60 K using laser pulsing under a DC voltage of 1–4 kV. Typically, 10–15 million atoms were collected.

X-ray diffraction (XRD, PANalytical/Philips X'pert MRD system) was performed in the ND direction on the RD–TD plane using a 1 mm × 1 mm beam. The Ag and Cu crystallite diameters were estimated using the Scherrer equation.[54] The anisometric shapes of Cu grains and Ag particles in the samples require measurements in perpendicular directions to define an average sphere-equivalent diameter. The Ag in-plane diameters after HPT were determined from the HAADF-STEM images in the RD–TD plane by measuring over 200 particles. The Cu grain in-plane diameters were determined using the linear intercept method[55] performed on BF-STEM images. XRD was performed such that it was primarily probing the thickness (ND) of the particles, and the values quoted from XRD measurements were found to be in good agreement with several cross-sectional STEM-based measurements. Both Ag and Cu average diameters reported in this study after HPT were calculated by combining the two sets of data, i.e., $D_p = \sqrt[3]{\left(D_{STEM}^2\right) \cdot D_{XRD}}$ to account for the anisometric particle and grain shapes. Additional HAADF-STEM images were taken in TD–ND planes, or RD direction, on selected samples to investigate more carefully the 3D shapes of the Ag precipitates. The particle and grain sizes measured entirely by HAADF-STEM were consistent with XRD/in-plane TEM analysis of crystallite size, supporting the validity of the approach used to calculate average diameters. This analysis was also applied to BM powders, which were composed primarily of millimeter-sized, disk-shaped alloy particles. Note that in subsequent discussion, precipitate diameter and grain diameter measured as described above will be distinguished from "crystallite diameter", measured solely from XRD performed primarily through thickness, ND. The solubility was estimated from the shift of the Cu(111) peak using a modified Vegard's law according to the lattice parameters of rapidly quenched metastable Cu–Ag alloys.[56] All characterizations were performed on samples taken from a radial position of 2 mm, unless stated otherwise; at this location, the total strain is ~1500, and the strain rates corresponding to 0.1, 1, and 6 rpm samples are 0.1, 1, and 6.25 s^{-1}.

III. RESULTS

Figure 2 shows the effect of total strain at 200 and 300 °C on the Ag crystallite size, Cu crystallite size, and Ag solubility for samples with a $D_{p,i}$ of 122 nm deformed at 1 rpm. Steady-state Ag and Cu crystallite sizes and Ag solubility are established well below a strain of 1500. Figure 3 indicates that at 400 °C, with a strain of 1500 imposed at 6.25 s^{-1} strain rate, the microstructural length scales established during HPT are independent of the initial particle and grain size within experimental error. For example, the initial Ag particle sizes of $D_{p,i}$ = 31 ± 7 nm and $D_{p,i}$ = 252 ± 58 nm are coarsened or refined to 65 ± 19 nm and 75 ± 20 nm, respectively. Based on the above experimental observation that the samples with the largest and smallest grain and particle sizes investigated can refine or coarsen to the same steady-state microstructure by a strain of 1500, this value of strain was selected for all subsequent microstructural analysis to investigate self-organization as a function of temperature and strain rate at consistent levels of strain, and presumably one representing the steady-state.

HAADF STEM images in Fig. 4 show the effect of temperature on Ag particle size in the ND direction (RD–TD plane) of samples, $D_{p,i}$ = 122 nm, subjected to HPT at low (0.1 s^{-1}) and high (6.25 s^{-1}) strain rates at 200 and 300 °C. The bright features in the images are Ag rich, the gray background is the Cu-rich matrix, and

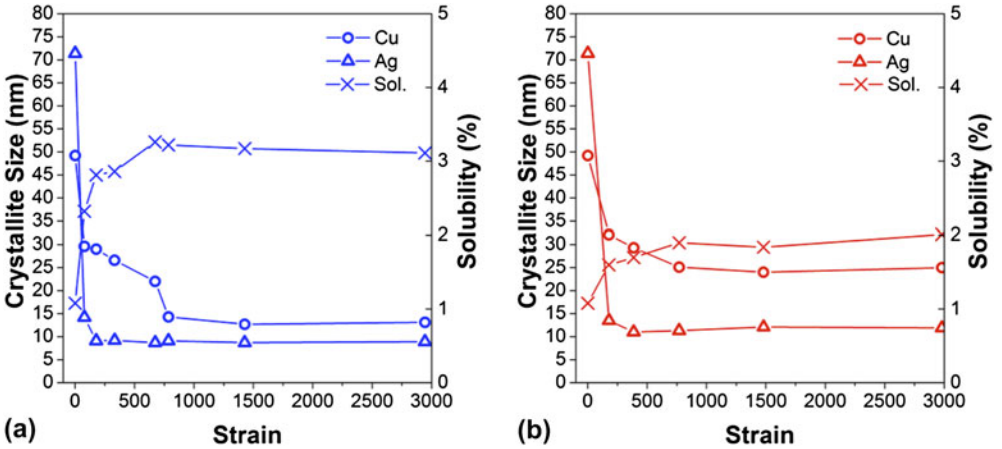


FIG. 2. Evolution of the Cu crystallite size, Ag crystallite size, and solubility with strain at (a) 200 and (b) 300 °C for the sample with a $D_{p,i}$ of 122 nm deformed at 1 rpm. All data estimated from XRD.

https://doi.org/10.1557/jmr.2015.119 Published online by Cambridge University Press

the low density of small dark features accordingly obtained from EDS measurements to be oxide particles (possibly associated with Fe contamination from the initial BM of the powder) and pores/bubbles (possibly due to Ar incorporation also from the initial BM). Reducing the temperature generally results in smaller Ag particles. At 125 °C, no distinct Ag particles were observed by HAADF-STEM.

Figure 5 summarizes the measurements of Ag particle diameters, Cu grain diameters, and Ag solubilities on samples processed at various strain rates and temperatures. The values associated with samples BM at temperatures nominally equivalent to the HPT temperatures are included for comparison, but for somewhat longer times, ≈2 h. Both the sphere-equivalent average Ag particle and Cu grain sizes increase with temperature

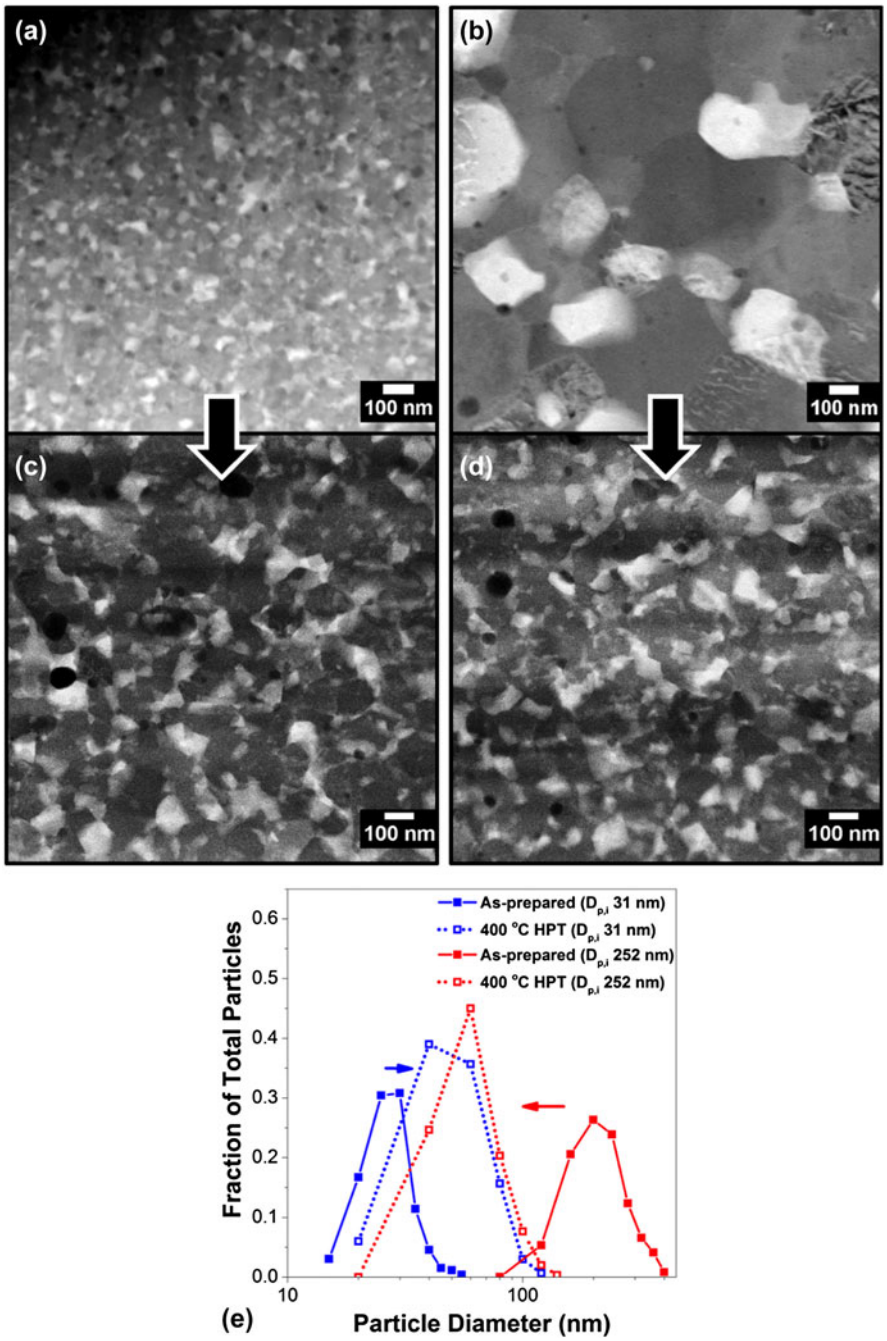


FIG. 3. (a and c) HAADF-STEM images of the sample with $D_{p,i}$ = 31 nm and (b and d) $D_{p,i}$ = 252 nm before and after 25 cycles of HPT at 400 °C at 6.25 s^{-1} strain rate, respectively. The images c and d are taken in the RD–TD plane. (e) Particle size distributions before and after HPT for the two samples.

https://doi.org/10.1557/jmr.2015.119 Published online by Cambridge University Press

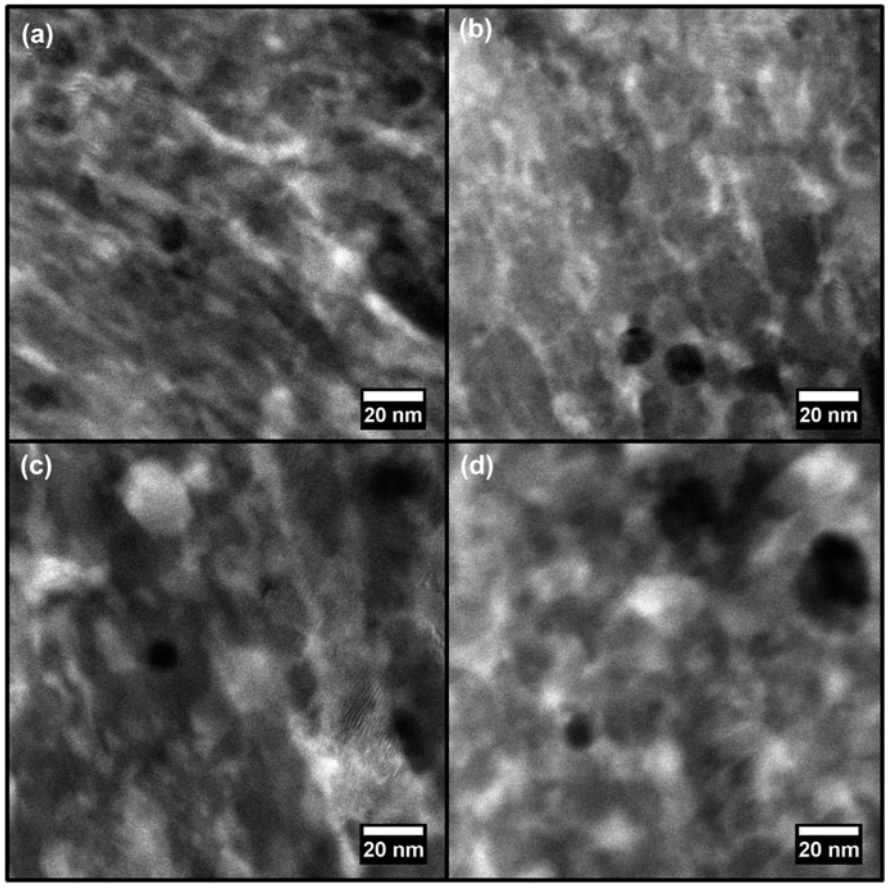


FIG. 4. HAADF-STEM images of the sample with $D_{p,i}$ = 122 nm after 25 cycles of HPT at 200 °C at (a) 0.1 s^{-1} and (b) 6.25 s^{-1}, and at 300 °C at (c) 0.1 s^{-1} and (d) 6.25 s^{-1}. All images are taken in the ND direction (RD–TD plane).

and exhibit negligible strain rate dependence, within experimental error. With the possible exception of one of the samples processed at 125 °C, the Ag solubility in Cu is relatively insensitive to strain rate. The grain and particle shapes, on the other hand, do display a strain-rate dependence, which will be discussed in more detail below. The Ag particle and Cu grain sizes in the BM samples are consistent with samples processed by HPT. The Ag solubility values, primarily deduced from the shift in the Cu(111) peak measured by XRD, for BM and HPT samples differ somewhat, primarily around 200 °C. The differences can be rationalized by small differences in processing temperatures, which are difficult to accurately measure during BM. Nevertheless, the trend of increasing Ag solubility with decreasing processing temperature is consistent across both data sets. The Ag solubilities in Cu determined from XRD were also confirmed for selected samples using APT, which provides a more sensitive measure of local solute concentration; this will be described in more detail below.

For samples deformed by HPT at 400 °C, the shapes of the Cu grains and Ag particles vary with strain rate, as seen in the HAADF-STEM images in the RD direction provided in Fig. 6. At the lowest strain rate, the Ag particles and Cu grains are most anisometric, on average exhibiting elongated morphologies aligned approximately perpendicular to the sample normal. At the highest strain rate, the Ag and Cu grains are far more equiaxed. The average ratio of Ag particle lengths parallel and perpendicular to the strain axis at 400 °C is 3.7, 2.1, and 1.4 at 0.1, 1, and 6.25 s^{-1}, respectively. This effect is also observed at 300 °C, as shown in Fig. 7, although its magnitude is somewhat smaller, with the average aspect ratio changing from 1.8 to 1.4 for strain rates increasing from 0.1 to 6.25 s^{-1}. Surprisingly, when imaged in the ND direction, the grains and particles in all samples appear equiaxed, suggesting that the elongated grains and particles observed at lower strain rates, on average, exhibit a plate-like morphology, compressed along the loading axis. The compressional strain of the samples, as noted above, was only ≈20% and cannot explain this behavior. Similar behavior was reported by Ren et al.[36] for large strains induced by mechanical wear.

Selected APT data were acquired to confirm the Ag solubility measurements determined from XRD, but also

https://doi.org/10.1557/jmr.2015.119 Published online by Cambridge University Press

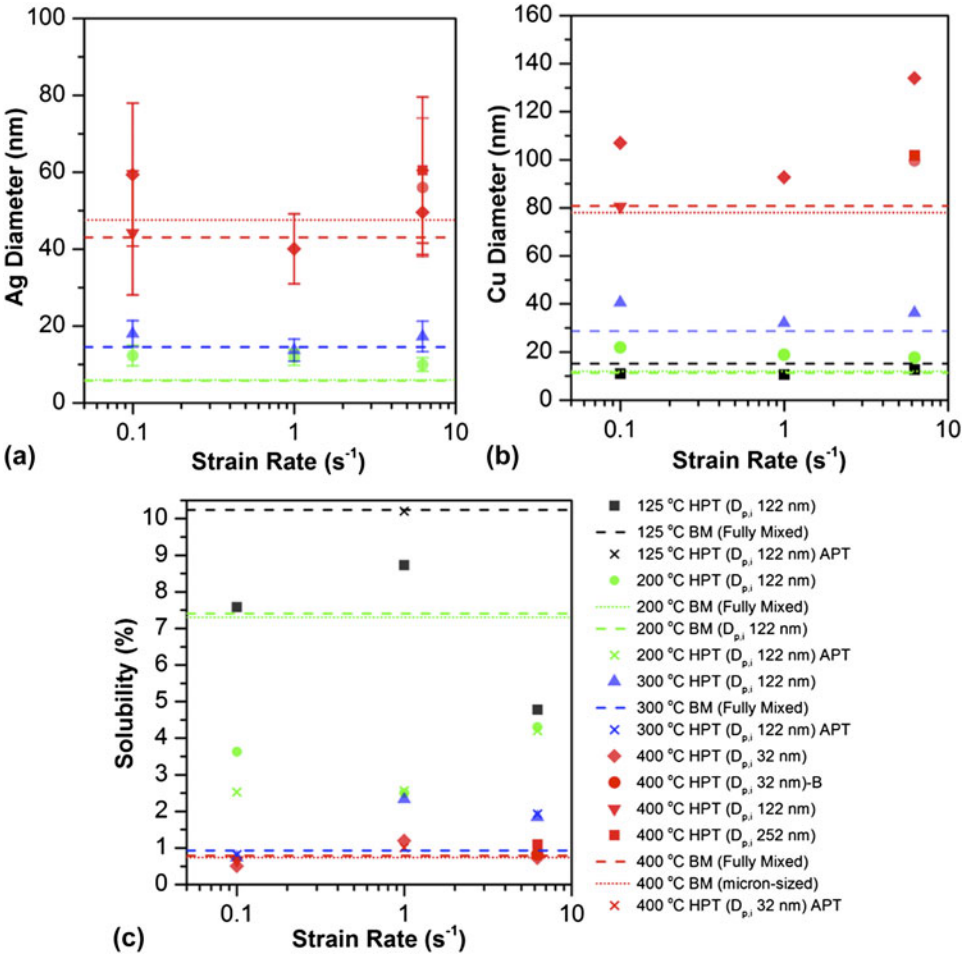


FIG. 5. (a) Ag particle and (b) Cu grain diameters calculated from the in-plane STEM images and corrected for thickness by XRD measurement, and (c) solubility of Ag in Cu (all data determined from the Cu(111) peak shift in XRD except the 'x' labels which is from APT). The dashed lines correspond to data taken from high temperature BM experiments. The legend applies to all three plots, and the parenthetical information describes the initial Ag particle size.

to characterize more broadly the Ag distribution in the different types of samples. Figure 8(a) shows reconstructed images of APT tips, where the color scale is based on the local average Ag concentration. These concentration maps were obtained by forming a simple cubic lattice with a cell size of 1 nm^3 and measuring the atomic concentration in each cell, or "voxel." Each voxel contains ≈100 atomic sites, although with the collection efficiency of the APT being ≈½, the average count/voxel was 42. Also shown in this figure is the distribution of Ag concentrations in all of the voxels. The dotted line represents the (Poisson) distribution for a homogeneous sample. At room temperature, the sample with $D_{p,i}$ = 122 nm chemically randomizes at strains exceeding 500 as reported in Ref. 17. The solubility of Ag in the Cu matrix was obtained by averaging the Ag concentration in voxels located away from the Ag precipitates. Figure 8(b), for example, shows the distributions of Ag in such regions under different HPT conditions. The results for the solubilities are presented in Table I. Overall, these results agree well with the data from XRD: the solubilities decrease with increasing temperature, while on the other hand, they have only a weak dependence on strain rate. It is noteworthy that at 125 °C no distinct Ag-rich particles larger than 1 voxel are present; consequently our procedure yields a solubility equal to the average concentration of Ag in the sample. The distribution, however, deviates from a Poisson distribution indicating that it is not completely random. To reflect the nonrandom distribution of Ag, and the observation of Ag rich voxels, subsequent discussion will assume that at 125 °C some Ag clustering occurs at a length scale of ≈1 nm, particularly, in the context of comparing the relationship between particle size and solubility.

At 200 °C, Ag particles are clearly observed, although they have relatively diffuse interfaces when compared to the samples prepared at 300 °C, as shown

https://doi.org/10.1557/jmr.2015.119 Published online by Cambridge University Press

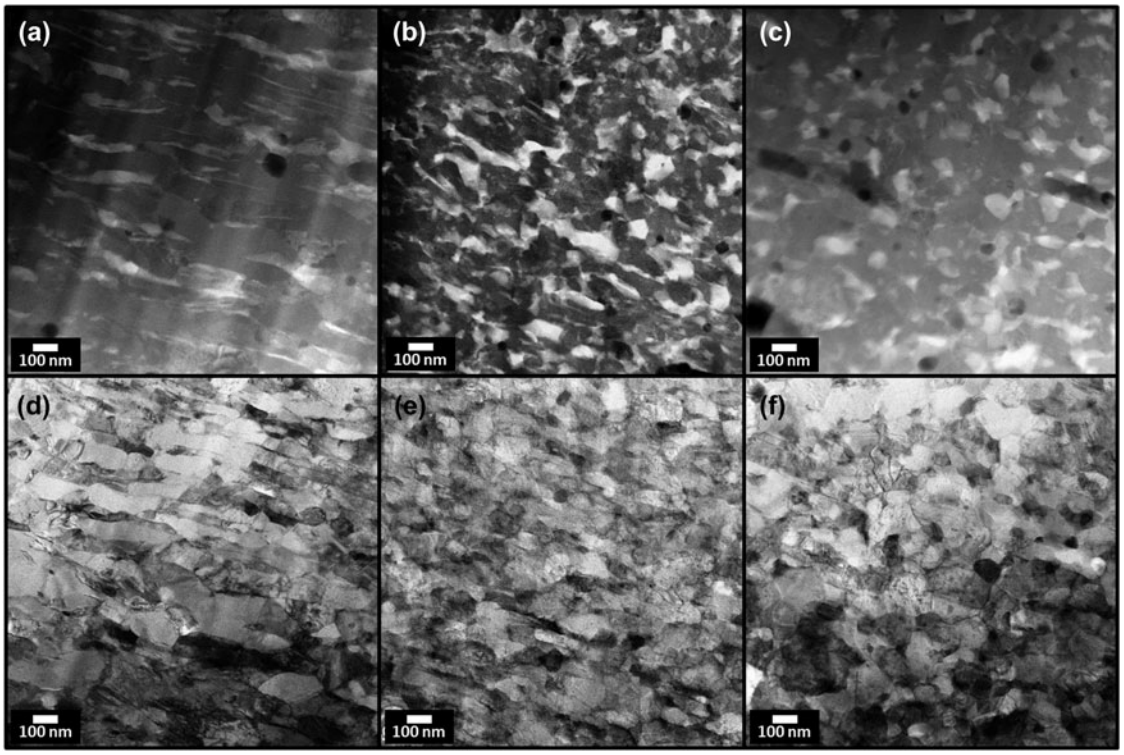


FIG. 6. HAADF-STEM images of the sample with $D_{p,i}$ = 31 nm sample after 25 cycles of HPT at 400 °C deformed at (a) 0.1 s^{-1}, (b) 1 s^{-1}, and (c) 6.25 s^{-1}, and their corresponding BF-STEM images (d, e, and f), respectively.

in Fig. 8(c). At 400 °C, no particles were observed, but this is due to the average interparticle distance exceeding the size of the APT tip. Interesting is that within the 400 °C sample, interconnected planes of Ag rich material are observed, possibly indicating Ag segregation to the Cu grain boundaries. APT also revealed Fe and O contamination, typically less than 0.1 and 1 at.%, respectively.

IV. DISCUSSION

Self-organization in A–B alloys with thermo-chemical properties similar to Cu–Ag during SPD had been investigated previously using KMC simulations.[47,57] These simulations predict how the microstructural length scales and nonequilibrium solubilities in these alloys depend on temperature and strain rate, and thus they provide a useful context to interpret the current experimental results. Before comparing these simulations with our experiments, however, the key assumptions in the model deserve comment. First, the KMC simulation uses a rigid lattice so it excludes any effects of grain boundaries, interphase boundaries, or interactions between dislocations. Thus, the model neglects shear-induced vacancy production, for example, by the non-conservative motion of jogs in screw dislocations,[58,59] even though past BM experiments indicate their potential importance.[13,45] This concentration of excess vacancies, moreover, is sensitive to temperature and various microstructural features,[58,60] and this makes accounting for them challenging in simulations. The KMC model, therefore, ignored shear-induced vacancies and simply used a single vacancy to mediate thermal diffusion, with the thermal vacancy concentration being accounted for by varying the vacancy jump frequency. Finally, the model assumes random shearing, i.e., a dislocation is forced to glide across the sample on one slip plane, and then a new dislocation is forced to glide on another of the 12 slip systems of the FCC lattice, which is chosen randomly. While these assumptions clearly obviate *direct* comparison between the simulations and experiments, the main predictions of the simulations are nevertheless quite useful for understanding the current experiments. Namely, the simulations provide a direct relationship between the microstructural length scale of the alloy, r, and the ratio of vacancy jump frequency to the frequency of shear-induced atomic relocations; as noted above $r = \frac{a_0}{d^2}\frac{F_{vac}}{F_{shear}}$. This relationship is clearly valid regardless of the source of vacancies: equilibrium vacancies or shear induced vacancies. We can relate this finding to the experiments by noting that,[47] $D_{vac} = \frac{2F_{vac}a_0^2}{d^3}$ and $D_{shear}(r) = \frac{a_0^2 \cdot F_{shear}}{d} \cdot \left(\frac{r}{a_0}\right)$, so that

https://doi.org/10.1557/jmr.2015.119 Published online by Cambridge University Press

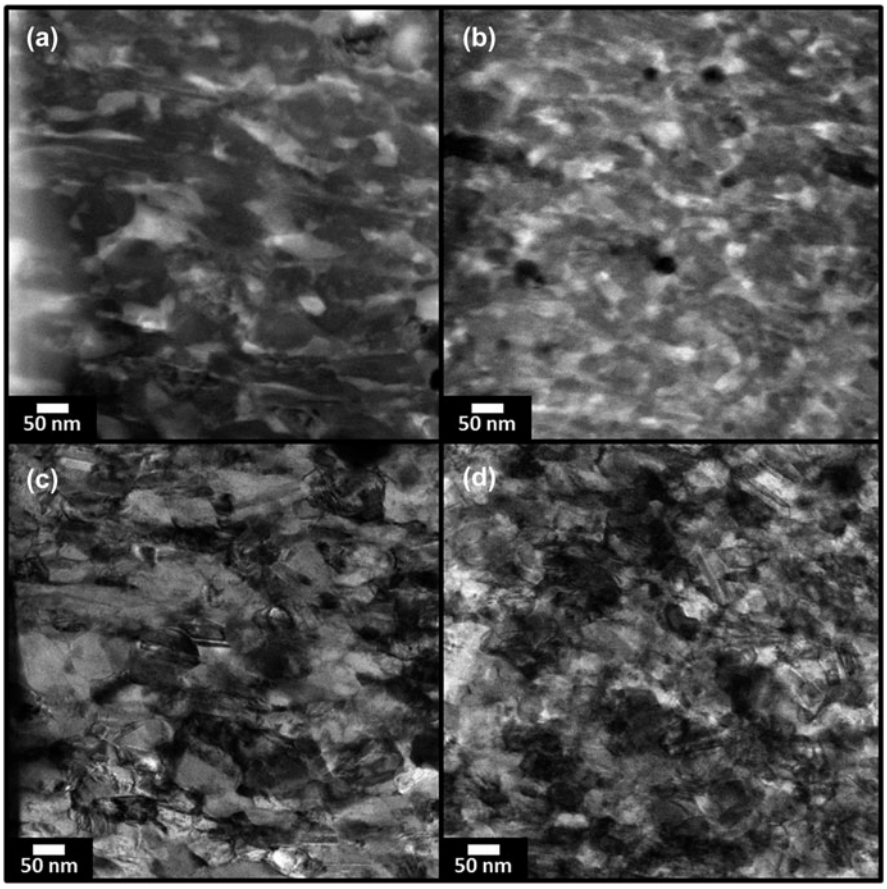


FIG. 7. HAADF-STEM images of the sample with $D_{p,i}$ = 122 nm sample after 25 cycles of HPT at 300 °C deformed at (a) 0.1 s^{-1} and (b) 6.25 s^{-1}, and their corresponding BF-STEM images (c and d), respectively.

$$r = \frac{a_0}{d^2}\frac{F_{vac}}{F_{shear}} = \frac{\nu c_v}{\dot{\gamma}} a_0 \quad , \qquad 1(a)$$

where c_v is the molar fraction of vacancies, ν is the frequency at which an individual vacancy jumps, and $\dot{\gamma}$ is the strain rate. The simulations also show that the solubility of an immiscible alloying addition during shear is governed by kinetic effects rather than thermodynamic (i.e., the Gibbs–Thomson equation). This leads to a characteristic scaling between solubility and microstructural length scale, also independent of the temperature and/or strain rate, and this scaling can be tested directly in the experiments.[47]

We begin our discussion by showing in Fig. 9 the results of the experiments and simulations on the same plot. The first feature to notice is that over a wide range of temperature (400–600 K), strain rate (10^{-11} s^{-1}–10^{-3} s^{-1}), and composition (15–50 at.%), the microstructural lengths in the simulations scale very well with $\frac{a_0}{d^2}\cdot\frac{F_{vac}}{F_{shear}}$. This provides strong support that Eq. (1) is fairly robust, being insensitive to the details of the microstructure and the concentration of vacancies. The experimental data are more difficult to plot since we do not know the vacancy jump frequency, *apriori*, however, since the length scale does not depend on strain rate, we show the experimental data in this plot as horizontal lines for the different temperatures. The reason for this lack of a dependence of r on strain rate can be understood by assuming that the vacancies are created solely by shear deformation, with each unit of strain producing a fixed concentration of vacancies, α, i.e., $dc_v^{shear}/dt = \alpha\dot{\gamma}$. If we further assume that these excess vacancies annihilate at grain boundaries, then $F_v^{shear} \propto \alpha\dot{\gamma}L^2/3\pi^2$, where L is the grain size. Since F_{shear} is also proportional to the strain rate, $\dot{\gamma}$, the ratio F_v/F_{shear} is independent of strain rate. These considerations also show why the experimental values of r are only weakly dependent on temperature, as r depends on temperature only through the grain size, L, where the experimental values show increases only slowly with temperature. Indeed, the increases in the experimental values of r with temperature shown in Fig. 9(a) are consistent with the increases in grain size shown in Fig. 5. This argument of first-order defect kinetics had been used previously to help explain phase stability in

https://doi.org/10.1557/jmr.2015.119 Published online by Cambridge University Press

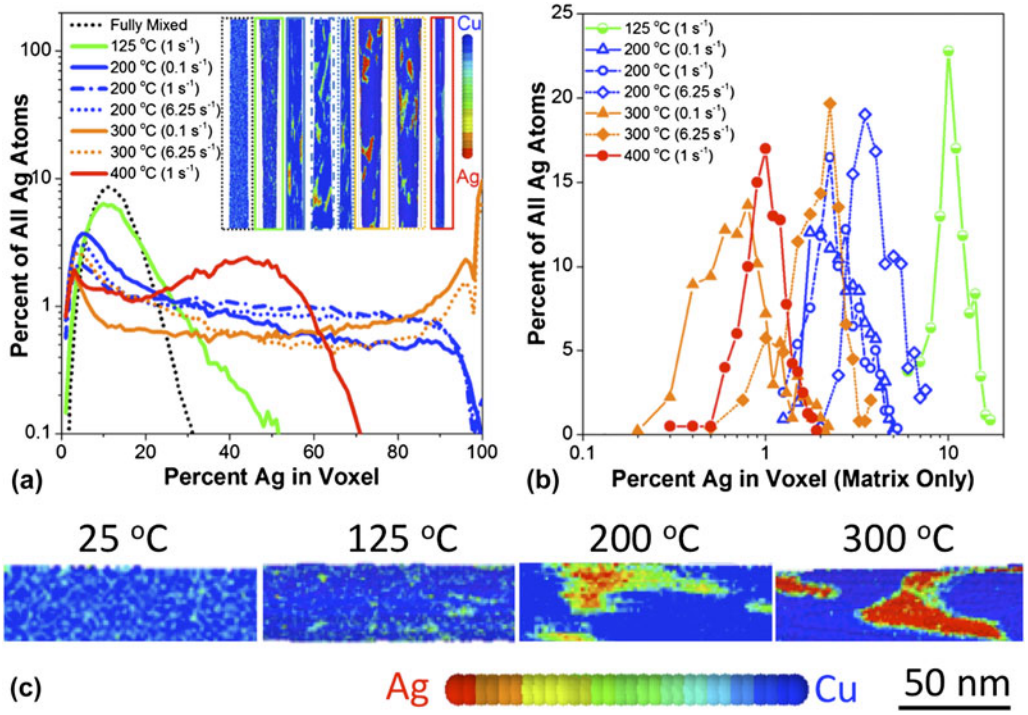


FIG. 8. (a) Distribution of Ag atoms versus percent Ag in voxels for different temperatures and deformation rates. The inset show 1 nm^3 voxel-based reconstruction of the tips corresponding to each plot. Data for fully mixed (random) sample are shown from previous study.[17] (b) Percent of all Ag atoms versus percent Ag in voxels located in the Cu-rich matrix region only (10 ,000–20,000 atoms in each distribution). (c) Voxel reconstructions of regions showing individual particles in the APT samples.

TABLE I. Solubilities in at.% as a function of temperature and strain rate measured from APT data along with values calculated from XRD (in parentheses).

Temp./strain rate (s^{-1})	125 °C	200 °C	300 °C	400 °C
0.1	(7.6)	2.5(3.6)	0.8(0.8)	(0.5)
1	10.2(8.7)	2.6(2.5)	(2.4)	1.0(1.2)
6	(4.8)	4.2(4.2)	1.9(2.0)	(0.9)

amorphous/crystalline NiZr alloys[61] and macroscopic phase separation in Cu/Ag alloys[13] during high temperature BM.

We next estimate the steady-state, shear-induced vacancy concentration. While, in principle, this can be directly achieved using Eq. (1a), the determination of the jump frequency of vacancies is difficult to estimate owing to correlation of jumps at interface (Cu/Ag) boundaries. We therefore compare the values r between the experiments and simulations at the same strain rate and temperature, i.e., $c_v^{shear} = \left(r_{exp}/r_{KMC}\right) \cdot c_v^{eq}$, where c_v^{eq} is the equilibrium vacancy concentration calculated in the simulations[62] and r_{exp} and r_{KMC} are the experimental and KMC values of the precipitate size, respectively. The values of c_v^{shear} obtained in this way are shown in Table II for the different temperatures used in the experiments, and as seen, they are on the order of 10^{-7}–10^{-3}. The highest concentration obtained, which occurs at the lowest temperature, $T = 200$ °C, is approximately a factor of 10 larger than the equilibrium concentration of vacancies at the melting temperature of Cu. If we assume further that the vacancies annihilate predominantly at grain boundaries, we can also estimate the vacancy production rate. We obtain for both 200 and 300 °C, $\alpha = 1.5 \times 10^{-3} \pm 6 \times 10^{-4}$. For comparison, we note the theoretical estimate of Mecking and Estrin,[60] $\alpha = 0.1\frac{\sigma}{G \cdot b^3}$, and with a value of $\sigma \approx 1$ GPa,[63] $\alpha = 3 \times 10^{-3}$. This close agreement with the experiments is clearly somewhat fortuitous, given the assumptions involved, but nevertheless, the agreement does show that the analysis provides physically reasonable estimates.

We can also compare the equilibrium concentration of vacancies (in pure Cu) at 400 °C, $c_v^{eq} \approx 1 \times 10^{-9}$ to the calculated shear-induced concentration $c_v^{shear} \approx 3 \times 10^{-7}$ (obtained at the lowest strain rate). The concentration of thermal vacancies is beginning to approach the shear induced concentration, and this perhaps explains why the precipitate size during thermal annealing at 400 °C is comparable to that during shear mixing at that temperature, as shown in Table III. As discussed below, however, recrystallization is also becoming active at this temperature, and this may also influence the behavior. Extrapolation of the nonequilibrium vacancy concentration to

https://doi.org/10.1557/jmr.2015.119 Published online by Cambridge University Press

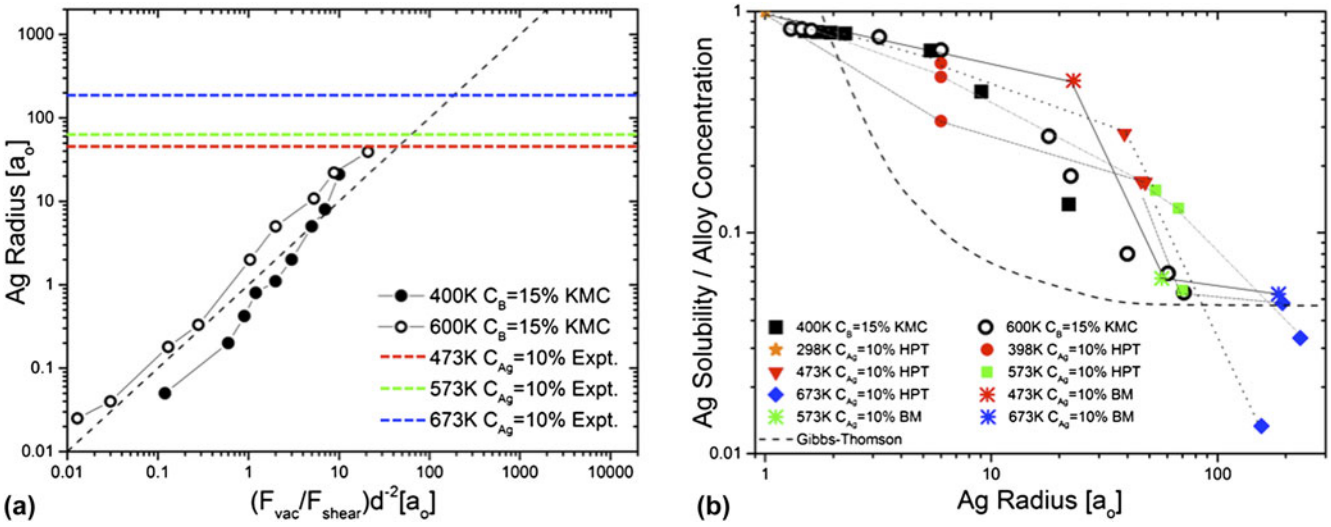


FIG. 9. (a) Comparison of microstructural length scale measured experimentally and calculated by KMC[47] as a function of the calculated thermal vacancy jump frequency normalized to the shearing frequency, d^2, and a_0. The experimental data are plotted as lines since the absolute vacancy concentration is not known explicitly. (b) Comparison of the solubility of Ag in Cu, normalized to Ag concentration, as a function of microstructural length scale measured experimentally ($Cu_{90}Ag_{10}$) and calculated by KMC ($Cu_{85}Ag_{15}$).[47] The dotted lines connect data points collected at equivalent strain rates.

125 °C shows that the concentration would be on the order of 10^{-2}. This is comparable to or exceeds the maximum excess concentration of vacancies that a crystal can support ($\approx 10^{-3}$–10^{-2}).[45] This explains why the microstructural length scale is markedly reduced at 125 °C despite the fact that vacancies are still mobile at this temperature (see Fig. 10); i.e., the vacancy concentration saturates and the effective production rate of nonequilibrium vacancies, α, is no longer independent of temperature. Wu et al.[45] assumed such behavior to explain the steady-state length scale in BM $Cu_{50}Ag_{50}$ between 120 and 180 °C.

The dependence of solubility is plotted in Fig. 9(b) as a function of length scale. In this case, the experiments and KMC simulations can be compared directly, and it is seen that they are in rough agreement. Both show much higher solubility at small length scales than does Gibbs–Thomson, but they approach Gibbs–Thomson, as calculated in Ref. 47, at large length scales. The fact that the relationship between solubility and microstructural length scale approaches Gibbs–Thomson at 400 °C suggests that the system is approaching equilibrium, in agreement with our estimates of c_v^{shear}/c_v^{eq} discussed above.

Finally, we consider the steady-state response of the system at 400 °C. At this temperature, the steady-state Ag particle size is characteristically larger than what would be extrapolated from lower temperatures in the Arrhenius plot shown in Fig. 10, thus suggesting a different mechanism influencing the process at 300 and 400 °C. Indeed for pure Cu, it has been predicted that at a strain rate of 0.1 s^{-1}, the transition from recovery to recrystallization will occur

TABLE II. Vacancy concentration (in atom fraction) as a function of strain rate and temperature calculated from our experimental data following Eq. (1).

	0.1 s^{-1}	1 s^{-1}	6.25 s^{-1}
473 K	3.1×10^{-5}	3.0×10^{-4}	1.6×10^{-3}
573 K	1.3×10^{-6}	1.0×10^{-5}	7.8×10^{-5}
673 K	3.6×10^{-7}	2.4×10^{-6}	1.9×10^{-5}

TABLE III. Comparison of samples thermally annealed and HPT at 400 °C for equivalent times. Note that the 4 min sample is at the highest strain rate and the 250 min sample is at the lowest strain rate.

Processing time	4 min	25 min	250 min
Ag particle size from thermal annealing at 400 °C	29 ± 6	38 ± 7	66 ± 16
Ag particle size from straining to 1500 at 400 °C	50 ± 11	39 ± 8	59 ± 19

at ≈380 °C.[64] Hong and Kwon[65] also observed recrystallization of $Cu_{84}Ag_{16}$ alloys at a strain rate of $\approx 10^{-4}$ at 400 °C, while they reported almost no recrystallization occurred in samples strained at 300 °C. Since the tracer diffusivity of Ag in Cu exceeds self-diffusion by an order of magnitude at these low temperatures, we will assume that grain growth and recrystallization of the primary Cu phase govern the evolution of grain shape. The significant differences in grain anisometry as a function of strain rate at 400 °C, *viz.*, becoming more equiaxed with increasing strain rate, suggest the onset of dynamic recrystallization. Samples processed at higher strain rates acquire stored energy more

https://doi.org/10.1557/jmr.2015.119 Published online by Cambridge University Press

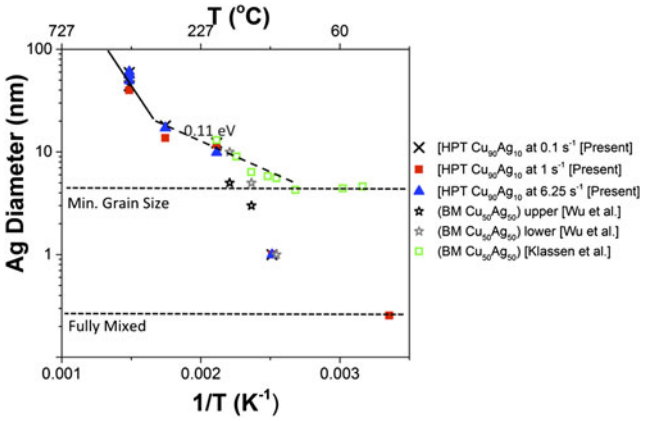


FIG. 10. Plot of Ag particle size as a function of temperature and strain rate comparing the current results with prior work utilizing $Cu_{50}Ag_{50}$ processed by BM.

quickly; thus promoting a higher nucleation rate of recrystallized grains and a more equiaxed structure. An increase in local sample heating due to higher strain rates[49] might also promote an increase in nucleation rate, although no significant temperature rise was observed at the anvils adjacent to the sample. BF-STEM images in Figs. 6 and 7 indicate a higher dislocation density within the grains of samples processed at 300 °C relative to those HPT at 400 °C, which is again consistent with a change in relaxation mechanism from dynamic recovery to dynamic recrystallization.

V. CONCLUSIONS

We have used HPT experiments at high temperatures to analyze the effects of temperature and strain rate on self-organization in dilute Cu–Ag. It was demonstrated that the same steady-state is achieved regardless of initial microstructure; coarse grained and decomposed or homogenized. The characteristic length scale associated with compositional patterning is approximately independent of shearing rate, and it shows a very low apparent activation energy. Experimental observations suggest that below 300 °C the excess nonequilibrium shear-induced vacancy concentration governs diffusional relaxations during high temperature shearing. A transition from recovery controlled coarsening to dynamic recrystallization dominated coarsening occurs between 300 and 400 °C. Self-organization reactions still prevail during dynamic recrystallization, but with strain rate primarily influencing particle and grain shapes.

ACKNOWLEDGMENTS

The authors would like to acknowledge the financial support from National Science Foundation (DMR 10-05813) to carry out this research. The APT was performed at the Northwestern University Center for Atom-Probe Tomography (NUCAPT), which is supported by the National Science Foundation's MRSEC Program (DMR-1121262). The research at TUD and KIT was financially supported by Deutsche Forschungsgemeinschaft (HA1344/22-2). The Austrian Science Fund FWF within the project No T512-N20 is thankfully acknowledged for supporting D.S.

REFERENCES

1. A. Gholinia, P.B. Prangnell, and M.V. Markushev: The effect of strain path on the development of deformation structures in severely deformed aluminum alloys processed by ECAE. *Acta Mater.* **48**(5), 1115 (2000).
2. K. Nakashima, Z. Horita, M. Nemoto, and T.G. Langdon: Influence of channel angle on the development of ultrafine grains in equal-channel angular pressing. *Acta Mater.* **46**(5), 1589 (1998).
3. N. Tsuji, Y. Saito, S-H. Lee, and Y. Minamino: ARB (accumulative roll-bonding) and other new techniques to produce bulk ultrafine grained materials. *Adv. Eng. Mater.* **5**(5), 338 (2003).
4. R. Valiev: Nanostructuring of metals by severe plastic deformation for advanced properties. *Nat. Mater.* **3**(8), 511 (2004).
5. A. Bachmaier, M. Kerber, D. Setman, and R. Pippan: The formation of supersaturated solid solutions in Fe–Cu alloys deformed by high-pressure torsion. *Acta Mater.* **60**(3), 860 (2012).
6. M. Dao, L. Lu, R.J. Asaro, J.T.M. De Hosson, and E. Ma: Toward a quantitative understanding of mechanical behavior of nanocrystalline metals. *Acta Mater.* **55**(12), 4041 (2007).
7. B.L. Huang, R.J. Perez, E.J. Lavernia, and M.J. Luton: Formation of supersaturated solid solutions by mechanical alloying. *Nanostruct. Mater.* **7**(1–2), 67 (1996).
8. J.Y. Huang, Y.D. Yu, Y.K. Wu, D.X. Li, and H.Q. Ye: Microstructure and nanoscale composition analysis of the mechanical alloying of FeXCu100-X (X = 16, 60). *Acta Mater.* **45**(1), 113 (1997).
9. V.V. Popov, E.N. Popova, and A.V. Stolbovskiy: Nanostructuring Nb by various techniques of severe plastic deformation. *Mater. Sci. Eng., A* **539**, 22 (2012).
10. X. Quelennec, A. Menand, J.M. Le Breton, R. Pippan, and X. Sauvage: Homogeneous Cu–Fe supersaturated solid solutions prepared by severe plastic deformation. *Philos. Mag.* **90**(9–10), 1179 (2010).
11. C.A. Schuh, T.G. Nieh, and H. Iwasaki: The effect of solid solution W additions on the mechanical properties of nanocrystalline Ni. *Acta Mater.* **51**(2), 431 (2003).
12. R.B. Schwarz and C.C. Koch: Formation of amorphous alloys by the mechanical alloying of crystalline powders of pure metals and powders of pure metals and powders of intermetallics. *Appl. Phys. Lett.* **49**(3), 146 (1986).
13. T. Klassen, U. Herr, and R.S. Averback: Ballmilling of systems with positive heat of mixing: Effect of temperature in Ag-Cu. *Acta Mater.* **45**(7), 2921 (1997).
14. F. Delogu, M. Pintore, S. Enzo, F. Cardellini, V. Contini, A. Montone, and V. Rosato: Mechanical alloying of immiscible elements: Experimental results on Ag-Cu and Co-Cu. *Philos. Mag. B* **76**(4), 651 (1997).
15. C. Gente, M. Oehring, and R. Bormann: Formation of thermodynamically unstable solid solutions in the copper-cobalt system by mechanical alloying. *Phys. Rev. B: Condens. Matter* **48**(18), 13244 (1993).

https://doi.org/10.1557/jmr.2015.119 Published online by Cambridge University Press

16. E. Ma and M. Atzmon: Phase transformations induced by mechanical alloying in binary systems. *Mater. Chem. Phys.* **39** (4), 249 (1995).
17. S.N. Arshad, T.G. Lach, M. Pouryazdan, H. Hahn, P. Bellon, S.J. Dillon, and R.S. Averback: Dependence of shear-induced mixing on length scale. *Scr. Mater.* **68**(3–4), 215 (2013).
18. M. Pouryazdan, D. Schwen, D. Wang, T. Scherer, H. Hahn, R.S. Averback, and P. Bellon: Forced chemical mixing of immiscible Ag-Cu heterointerfaces using high-pressure torsion. *Phys. Rev. B: Condens. Matter Mater. Phys.* **86**(14), 144302 (2012).
19. P. Bellon, R.S. Averback, S. Odunuga, Y. Li, P. Krasnochtchekov, and A. Caro: Crossover from superdiffusive to diffusive mixing in plastically deformed solids. *Phys. Rev. Lett.* **99**(11), 110602 (2007).
20. Y. Ashkenazy, N.Q. Vo, D. Schwen, R.S. Averback, and P. Bellon: Shear induced chemical mixing in heterogeneous systems. *Acta Mater.* **60**(3), 984 (2012).
21. J. Xu, U. Herr, T. Klassen, and R.S. Averback: Formation of supersaturated solid solutions in the immiscible Ni-Ag system by mechanical alloying. *J. Appl. Phys.* **79**(8, Pt. 1), 3935 (1996).
22. M. Wang, R.S. Averback, P. Bellon, and S. Dillon: Chemical mixing and self-organization of Nb precipitates in Cu during severe plastic deformation. *Acta Mater.* **62**, 276 (2014).
23. M. Wang, N.Q. Vo, M. Campion, T.D. Nguyen, D. Setman, S. Dillon, P. Bellon, and R.S. Averback: Forced atomic mixing during severe plastic deformation: Chemical interactions and kinetically driven segregation. *Acta Mater.* **66**, 1 (2014).
24. E. Ma, J.H. He, and P.J. Schilling: Mechanical alloying of immiscible elements: Ag-Fe contrasted with Cu-Fe. *Phys. Rev. B: Condens. Matter* **55**(9), 5542 (1997).
25. E. Botcharova, J. Freudenberger, and L. Schultz: Mechanical alloying of copper with niobium and molybdenum. *J. Mater. Sci.* **39**(16–17), 5287 (2004).
26. A. Da Pozzo, S. Palmas, A. Vacca, and F. Delogu: On the role of mechanical properties in the early stages of the mechanical alloying of $Ag_{50}Cu_{50}$ powder mixtures. *Scr. Mater.* **67**(1), 104 (2012).
27. Z.C. Cordero and C.A. Schuh: Phase strength effects on chemical mixing in extensively deformed alloys. *Acta Mater.* **82**, 123 (2015).
28. A.C. Lund and C.A. Schuh: Topological and chemical arrangement of binary alloys during severe deformation. *J. Appl. Phys.* **95**(9), 4815 (2004).
29. N.Q. Vo, S. Odunuga, P. Bellon, and R.S. Averback: Forced chemical mixing in immiscible alloys during severe plastic deformation at elevated temperatures. *Acta Mater.* **57**(10), 3012 (2009).
30. A. Hohenwarter, M. Faller, B. Rashkova, and R. Pippan: Influence of heat treatment on the microstructural evolution of Al-3 wt.% Cu during high-pressure torsion. *Philos. Mag. Lett.* **94**(6), 342 (2014).
31. X. Sauvage, N. Enikeev, R. Valiev, Y. Nasedkina, and M. Murashkin: Atomic-scale analysis of the segregation and precipitation mechanisms in a severely deformed Al-Mg alloy. *Acta Mater.* **72**, 125 (2014).
32. B.B. Straumal, A.S. Gornakova, O.B. Fabrichnaya, M.J. Kriegel, A.A. Mazilkin, B. Baretzky, A.M. Gusak, and S.V. Dobatkin: Effective temperature of high pressure torsion in Zr-Nb alloys. *High Temp. Mater. Processes (Berlin, Ger.)* **31**(4–5), 339 (2012).
33. B.B. Straumal, S.G. Protasova, A.A. Mazilkin, O.A. Kogtenkova, L. Kurmanaeva, B. Baretzky, G. Schutz, A. Korneva, and P. Zieba: SPD-induced changes of structure and magnetic properties in the Cu-Co alloys. *Mater. Lett.* **98**, 217 (2013).
34. K. Tugcu, G. Sha, X.Z. Liao, P. Trimby, J.H. Xia, M.Y. Murashkin, Y. Xie, R.Z. Valiev, and S.P. Ringer: Enhanced grain refinement of an Al-Mg-Si alloy by high-pressure torsion processing at 100 °C. *Mater. Sci. Eng., A* **552**, 415 (2012).
35. A.P. Zhilyaev, S.N. Sergeev, and T.G. Langdon: Electron backscatter diffraction (EBSD) microstructure evolution in HPT copper annealed at a low temperature. *J. Mater. Res. Technol.* (2014). Ahead of print.
36. F. Ren, S.N. Arshad, P. Bellon, R.S. Averback, M. Pouryazdan, and H. Hahn: Sliding wear-induced chemical nanolayering in Cu-Ag, and its implications for high wear resistance. *Acta Mater.* **72**, 148 (2014).
37. Y.Z. Tian, S.D. Wu, Z.F. Zhang, R.B. Figueiredo, N. Gao, and T.G. Langdon: Comparison of microstructures and mechanical properties of a Cu-Ag alloy processed using different severe plastic deformation modes. *Mater. Sci. Eng., A* **528**(13–14), 4331 (2011).
38. Y.Z. Tian, Z.F. Zhang, and T.G. Langdon: Achieving homogeneity in a two-phase Cu-Ag composite during high-pressure torsion. *J. Mater. Sci.* **48**(13), 4606 (2013).
39. Y.Z. Tian, J.J. Li, P. Zhang, S.D. Wu, Z.F. Zhang, M. Kawasaki, and T.G. Langdon: Microstructures, strengthening mechanisms and fracture behavior of Cu-Ag alloys processed by high-pressure torsion. *Acta Mater.* **60**(1), 269 (2012).
40. Y.Z. Tian, S.D. Wu, Z.F. Zhang, R.B. Figueiredo, N. Gao, and T.G. Langdon: Microstructural evolution and mechanical properties of a two-phase Cu-Ag alloy processed by high-pressure torsion to ultrahigh strains. *Acta Mater.* **59**(7), 2783 (2011).
41. Y. Saito, H. Utsunomiya, N. Tsuji, and T. Sakai: Novel ultra-high straining process for bulk materials-development of the accumulative roll-bonding (ARB) process. *Acta Mater.* **47**(2), 579 (1999).
42. R.Z. Valiev, I.V. Alexandrov, Y.T. Zhu, and T.C. Lowe: Paradox of strength and ductility in metals processed by severe plastic deformation. *J. Mater. Res.* **17**(1), 5 (2002).
43. C. Suryanarayana: Mechanical alloying and milling. *Prog. Mater. Sci.* **46**(1–2), 1 (2000).
44. S. Zghal, R. Twesten, F. Wu, and P. Bellon: Electron microscopy nanoscale characterization of ball milled Cu-Ag powders. Part II: Nanocomposites synthesized by elevated temperature milling or annealing. *Acta Mater.* **50**(19), 4711 (2002).
45. F. Wu, D. Isheim, P. Bellon, and D.N. Seidman: Nanocomposites stabilized by elevated-temperature ball milling of $Ag_{50}Cu_{50}$ powders: An atom probe tomographic study. *Acta Mater.* **54**(10), 2605 (2006).
46. S. Odunuga, Y. Li, P. Krasnochtchekov, P. Bellon, and R.S. Averback: Forced chemical mixing in alloys driven by plastic deformation. *Phys. Rev. Lett.* **95**(4), 045901 (2005).
47. D. Schwen, M. Wang, R.S. Averback, and P. Bellon: Compositional patterning in immiscible alloys subjected to severe plastic deformation. *J. Mater. Res.* **28**(19), 2687 (2013).
48. A.P. Zhilyaev and T.G. Langdon: Using high-pressure torsion for metal processing: Fundamentals and applications. *Prog. Mater. Sci.* **53**(6), 893 (2008).
49. P.H.R. Pereira, R.B. Figueiredo, Y. Huang, P.R. Cetlin, and T.G. Langdon: Modeling the temperature rise in high-pressure torsion. *Mater. Sci. Eng., A* **593**, 185 (2014).
50. R.Z. Valiev, R.K. Islamgaliev, and I.V. Alexandrov: Bulk nanostructured materials from severe plastic deformation. *Prog. Mater. Sci.* **45**(2), 103 (2000).
51. A. Einstein: Über die von der molekularkinetischen Theorie der Wärme geforderte Bewegung von in ruhenden Flüssigkeiten suspendierten Teilchen. *Ann. Phys.* **17**, 549 (1905).
52. G. Martin and P. Bellon: Driven alloys. *Solid State Phys.* **50**, 189 (1997).
53. O.C. Hellman, J.A. Vandenbroucke, J. Rusing, D. Isheim, and D.N. Seidman: Analysis of three-dimensional atom-probe data by the proximity histogram. *Microsc. Microanal.* **6**(5), 437 (2000).

https://doi.org/10.1557/jmr.2015.119 Published online by Cambridge University Press

54. A.L. Patterson: The Scherrer formula for X-Ray particle size determination. *Phys. Rev.* **56**(10), 978 (1939).
55. J.E. Hilliard: Conversion of intercept density to grain size. *Met. Prog.* **85**(5), 99 (1964).
56. R.K. Linde: Lattice parameters of metastable Ag-Cu alloys. *J. Appl. Phys.* **37**(2), 934 (1966).
57. R.A. Enrique and P. Bellon: Compositional patterning in systems driven by competing dynamics of different length scale. *Phys. Rev. Lett.* **84**(13), 2885 (2000).
58. M. Militzer, W.P. Sun, and J.J. Jonas: Modeling the effect of deformation-induced vacancies on segregation and precipitation. *Acta Metall. Mater.* **42**(1), 133 (1994).
59. S.H. Song, X.M. Chen, and L.Q. Weng: Solute diffusion during high-temperature plastic deformation in alloys. *Mater. Sci. Eng., A* **528**(24), 7196 (2011).
60. H. Mecking and Y. Estrin: The effect of vacancy generation on plastic deformation. *Scr. Metall.* **14**(7), 815 (1980).
61. Y. Chen, M. Bibole, R. Le Hazif, and G. Martin: Ball-milling-induced amorphization in Ni_xZr_y compounds: A parametric study. *Phys. Rev. B* **48**(1), 14 (1993).
62. The equilibrium vacancy concentration, like the vacancy jump frequency, is influenced by interphase boundaries, however, it has been calculated in the simulations.
63. N.Q. Vo, J. Schaefer, R.S. Averback, K. Albe, Y. Ashkenazy, and P. Bellon: Reaching theoretical strengths in nanocrystalline Cu by grain boundary doping. *Scr. Mater.* **65**(8), 660 (2011).
64. E.I. Galindo-Nava and P.E.J. Rivera-Diaz-del-Castillo: Thermostatistical modelling of hot deformation in FCC metals. *Int. J. Plast.* **47**, 202 (2013).
65. S.I. Hong and H.J. Kwon: Superplasticicity of Cu–16 at.% Ag microcomposites. *J. Mater. Res.* **16**(06), 1822 (2001).

https://doi.org/10.1557/jmr.2015.119 Published online by Cambridge University Press